

Effective two-body scatterings around a massive object

Yihan Wang,^{1,2*} Saavik Ford,^{4,5} Rosalba Perna,^{3,5} Barry McKernan,^{4,5} Zhaohuan Zhu^{1,2} and Bing Zhang^{1,2}

¹*Nevada Center for Astrophysics, University of Nevada, Las Vegas, NV 89154*

²*Department of Physics and Astronomy, University of Nevada Las Vegas, Las Vegas, NV 89154, USA*

³*Department of Physics and Astronomy, Stony Brook University, Stony Brook, NY 11794-3800, USA*

⁴*Department of Science, BMCC, City University of New York, New York, NY 10007, USA*

⁵*Center for Computational Astrophysics, Flatiron Institute, New York, NY 10010, USA*

Accepted XXX. Received YYY; in original form ZZZ

ABSTRACT

Two-body scatterings under the potential of a massive object are very common in astrophysics. If the massive body is far enough away that the two small bodies are in their own gravitational sphere of influence, the gravity of the massive body can be temporarily ignored. However, this requires the scattering process to be fast enough that the small objects do not spend too much time at distances near the surface of the sphere of influence. In this paper, we derive the validation criteria for effective two-body scattering and establish a simple analytical solution for this process, which we verify through numerical scattering experiments. We use this solution to study star-black hole scatterings in the disks of Active Galactic Nuclei and planet-planet scatterings in planetary systems, and calculate their one-dimensional cross-section analytically. Our solution will be valuable in reducing computational time when treating two-body scatterings under the potential of a much more massive third body, provided that the problem settings are in the valid parameter space region identified by our study.

Key words: Accretion disks – galaxies: active – black hole physics

1 INTRODUCTION

The study of two-body scatterings is a fundamental topic in physics that has been investigated for over a century. When two particles interact, they exchange energy and momentum, resulting in a change in their direction and speed. When such scattering events occur around a massive object, the particles can experience a gravitational deflection due to the object’s gravitational field, altering their impact parameter and scattering angle.

The concept of the gravitational sphere of influence was first introduced by Laplace to study close encounters between comets and Jupiter in our solar system. This sphere defines the region where the motion of objects is dominated by the gravity of a celestial body, and the gravity of other objects can be ignored temporarily. The radius of the sphere can be defined in several ways, such as Hill’s radius and Laplace’s radius, which depend solely on the masses of the objects involved.

Öpik (Ernst 1976) introduced a model for calculating the trajectories of asteroids following close encounters with planets. The model assumes encounters are instantaneous and that the gravity of the Sun can be temporarily ignored, which allows for the explicit expression of the post-encounter orbital parameters of the asteroid from two-body scattering with pre-encounter initial conditions. If the encounter is fast enough that the orbital deflection from the planet is negligible, Opik’s method works well over a wide range of parameter space. However, when orbital deflection from the planet is significant,

this method fails to accurately predict the post-encounter trajectories of the scattering objects.

Initially, Opik’s method was thought to be useful only when the impact parameter between the asteroid and the planet was smaller than the radius of the sphere of influence, and the two-body scattering model became invalid when the impact parameter was too large. However, later investigations (Greenberg et al. 1988; Carusi et al. 1990; Valsecchi et al. 1997) found that Opik’s method becomes less reliable because the pre-encounter deflection from the planet results in a different encounter geometry than originally assumed. However, if this deflection can be accurately calculated or a more solid velocity-dependent (implicitly or explicitly) sphere of influence can be used to validate the parameter space of Opik’s method, accurate analytical post-encounter trajectory predictions are still possible. The goal of this paper is to identify the accurate parameter space in which Opik’s method can be properly used and apply the method to several astrophysical phenomena to obtain analytical cross-sections for these events.

Fortunately, in many cases of astrophysical interest, we are in a regime that does permit analytic solutions that are valid to high accuracy. In particular, in the case of a star with planets or protoplanets in a disk, or the analogous situation of stars or stellar mass black holes in an active galactic nucleus (AGN) disk, the gas disk provides a preferred orientation for orbits around the central object.

Stars and stellar-origin BHs are expected to be found in the disks of AGNs, either due to in-situ formation (e.g. Stone et al. 2017) or due to capture from the nuclear star clusters (e.g. McKernan et al. 2012; Kennedy et al. 2016; Bartos et al. 2017; Fabj et al. 2020). Once in the disk, BHs and stars are subject to frequent dynamical interactions

* E-mail: yihan.wang@unlv.edu

(Samsing et al. 2020; Wang et al. 2021c), and our formalism allows us to easily identify regions of parameter space in which the outcome of the scattering is especially interesting. In particular, in the following we will consider in detail two cases: one in which the scattering leads to the tidal disruption of the star by the stellar mass BH (micro-TDE) (Perets et al. 2016; Kremer et al. 2022; Yang et al. 2020; Wang et al. 2021a; Ryu et al. 2022), and one in which the star gets scattered within the sphere of influence (for tidal disruption) of the central SMBH, hence giving rise to a standard tidal disruption event (TDE) (Rees 1988; Evans & Kochanek 1989; Phinney 1989).

The paper is structured as follows: in section 2 we describe the problem and the analytical solutions for the post-scattering trajectories, and present analytical formulas suitable for inclusion into N -body codes; we further test these formulas against numerical simulations. In section 3 we apply our results to two astrophysical scenarios: an AGN disk, for which we determine the rate of TDEs and micro-TDEs, and a protoplanetary/transition disk, where we determine the distribution of free-floating and highly eccentric planets. We finally summarize and discuss the caveats of our analysis in Sec.4.

2 HYPERBOLIC SCATTERINGS AROUND A MASSIVE OBJECT

2.1 Free two-body scattering and turning angle

To construct our formalism, we begin with free two-body scattering and we consider the turning angle after the encounter. The scattering object is assumed to be on a hyperbolic orbit with semi-major axis a_{hyp} , eccentricity e_{hyp} , and total energy of the two-body system > 0 . If we choose one of the objects as a reference frame, the distance of the other object to the origin can be written as

$$r_{\text{hyp}} = \frac{P}{1 + e_{\text{hyp}} \cos \theta}, \quad (1)$$

where $P = a_{\text{hyp}}(1 - e_{\text{hyp}}^2)$ is the semi-latus rectum, and θ is the true anomaly. $\theta = 0$ yields $r = a_{\text{hyp}}(1 - e_{\text{hyp}})$, which corresponds to the pericenter distance. Using energy conservation we can calculate the semi-major axis of the hyperbolic orbit. The specific total energy of the system at $t = -\infty$ is $v_{\infty}^2/2$, while the total specific energy of the Keplerian orbit is $-\mu_{12}/2a_{\text{hyp}}$, where $\mu_{ijk\dots} = G(m_i + m_j + m_k + \dots)$ is the gravitational constant of an N -body system. Therefore, from $\frac{v_{\infty}^2}{2} = -\frac{\mu_{12}}{2a_{\text{hyp}}}$, we get

$$a_{\text{hyp}} = -\frac{\mu_{12}}{v_{\infty}^2}. \quad (2)$$

The eccentricity of a conic section is given by

$$e_{\text{hyp}} = \sqrt{1 + b^2/a_{\text{hyp}}^2}, \quad (3)$$

where b is the impact parameter. Using Equation 1, we can calculate the corresponding $\theta(t)$ of $r_{\text{hyp}} = +\infty$,

$$\theta(\pm\infty) = \pm \arccos(1/e_{\text{hyp}}). \quad (4)$$

The turning angle of the hyperbolic trajectory, $\theta_{\text{turn}} = \pi - [\theta(+\infty) - \theta(-\infty)]$ can then be written as

$$\theta_{\text{turn}} = \pi - 2 \arccos\left(\frac{1}{e_{\text{hyp}}}\right). \quad (5)$$

Plugging in the semi-major axis and eccentricity a_{hyp} and e_{hyp} , we can finally express the turning angle as a function of v_{∞} and b ,

$$\theta_{\text{turn}} = 2 \arctan \frac{\mu_{12}}{v_{\infty}^2 b}. \quad (6)$$

2.2 Turning timescale

The time around the closest approach $\tau_{\text{turn}} = t(\theta = \pi/2) - t(\theta = -\pi/2)$ can be calculated as

$$\Delta t = \sqrt{-a_{\text{hyp}}^3/\mu_{12}} [M(t_f) - M(t_0)], \quad (7)$$

where $M(t)$ is the mean anomaly (the fraction of a Keplerian orbit's period that has elapsed) of the hyperbolic orbit. This corresponds to the time that the relative distance between m_1 and m_2 is smaller than $a_{\text{hyp}}(1 - e_{\text{hyp}}^2)$ (Later on, we will show that this is consistent with the well-known Hill's sphere of influence and our experiments find that this is a good approximation for the turning time). For $\theta = \pm\pi/2$, the corresponding $M(t)$ are

$$\begin{aligned} M_{\theta=\pi/2} &= e_{\text{hyp}} \sqrt{e_{\text{hyp}}^2 - 1} - \ln(e_{\text{hyp}} + \sqrt{e_{\text{hyp}}^2 - 1}) \\ &= f(e_{\text{hyp}}) \end{aligned} \quad (8)$$

$$M_{\theta=-\pi/2} = -e_{\text{hyp}} \sqrt{e_{\text{hyp}}^2 - 1} + \ln(e_{\text{hyp}} + \sqrt{e_{\text{hyp}}^2 - 1}), \quad (9)$$

respectively. Therefore, the timescale of the scattering event (timescale to turn) can be estimated as

$$\tau_{\text{turn}} = 2f(e_{\text{hyp}}) \sqrt{-a_{\text{hyp}}^3/\mu_{12}} = 2\sqrt{\frac{P^3}{\mu_{12}}} \frac{f(e_{\text{hyp}})}{(e_{\text{hyp}}^2 - 1)^{3/2}} = 2\sqrt{\frac{P^3}{\mu_{12}}} g(e_{\text{hyp}}). \quad (10)$$

The semi-latus rectum P can also be rewritten as $P = h^2/\mu_{12} = b^2 v_{\infty}^2/\mu_{12}$, where h is the specific angular momentum.

2.3 Effective two-body scattering in the potential of a third massive object

If the two-body scattering happens under the presence of a massive object, at the closest approach between the two light objects, the center of mass of these will undergo a nearly Keplerian motion around the massive object. The corresponding timescale of this motion is

$$\tau_{\text{orb}} = 2\pi \sqrt{r^3/\mu_{123}} \sim 2\pi \sqrt{r^3/\mu_3}, \quad (11)$$

where m_1 and m_2 are the masses of the light objects and m_3 the mass of the heavier one. Comparing this timescale with the turning timescale we obtained in the last subsection, we obtain the timescale ratio

$$\tau_{\text{turn}}/\tau_{\text{orb}} = \frac{g(e_{\text{hyp}})}{\pi} \left(\frac{\mu_3}{\mu_{12}}\right)^{1/2} \left(\frac{bv_{\infty}}{\sqrt{\mu_{12}r}}\right)^3. \quad (12)$$

If the ratio $\tau_{\text{turn}}/\tau_{\text{orb}}$ is small enough, the center of mass movements around the massive object can be safely ignored during the scattering process.

In the reference frame of the third massive body m_3 , before the scattering, if the velocity of m_1 is \mathbf{v}_1 and the velocity of m_2 is \mathbf{v}_2 , we can rewrite these velocities as

$$\mathbf{v}_1 = \frac{m_1 \mathbf{v}_1 + m_2 \mathbf{v}_2}{m_{12}} + \frac{m_2}{m_{12}} (\mathbf{v}_1 - \mathbf{v}_2) \quad (13)$$

$$\mathbf{v}_2 = \frac{m_1 \mathbf{v}_1 + m_2 \mathbf{v}_2}{m_{12}} + \frac{m_1}{m_{12}} (\mathbf{v}_2 - \mathbf{v}_1). \quad (14)$$

The first term in each equation is the center of mass velocity of m_1 and m_2 , while the second term represents the velocity in their centre of mass reference frame. If the condition

$$\tau_{\text{turn}}/\tau_{\text{orb}} \ll 1 \quad (15)$$

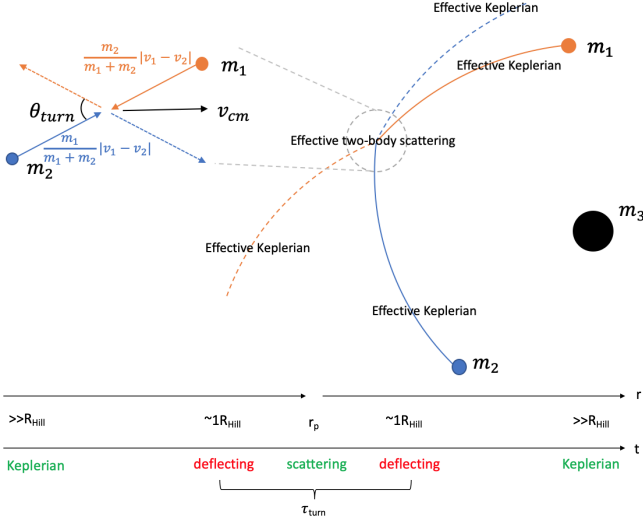


Figure 1. Schematics of effective two-body scattering theory. If $\tau_{\text{turn}}/\tau_{\text{orb}} \ll 1$, the scattering keeps the center of mass velocity \mathbf{v}_{cm} but turns the reduced velocity vectors by an angle of θ_{turn} .

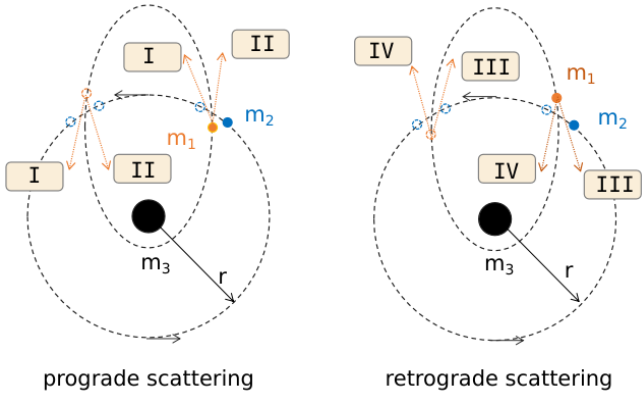


Figure 2. Schematics of disk-like two-body scatterings around massive object m_3 in Keplerian orbits. *Left:* panel shows the prograde scatterings where m_1 and m_2 orbit around m_3 in the same (**counter-clockwise**) direction. *Right:* panels shows the retrograde scatterings where m_2 orbits as before, but m_1 now orbits around m_3 in the opposite (**clockwise**) direction.

is satisfied, the motion of the center of mass of m_1 and m_2 can be safely ignored during the turning time. Therefore, during this time, only the second term of Equation 13 and 14 changes. As shown in Figure 1, in the centre of mass reference frame of m_1 and m_2 , due to energy and angular momentum conservation, the scattering maintains the magnitude of the velocities of m_1 and m_2 but turns them by an angle of θ_{turn} . Therefore, in the reference frame of m_3 , the velocity of m_1 and m_2 after the scattering can be expressed as

$$\mathbf{v}'_1 = \frac{m_1 \mathbf{v}_1 + m_2 \mathbf{v}_2}{m_{12}} + \frac{m_2}{m_{12}} (\mathbf{v}_1 - \mathbf{v}_2) \mathcal{R}(\theta_{\text{turn}}) \quad (16)$$

$$\mathbf{v}'_2 = \frac{m_1 \mathbf{v}_1 + m_2 \mathbf{v}_2}{m_{12}} + \frac{m_1}{m_{12}} (\mathbf{v}_2 - \mathbf{v}_1) \mathcal{R}(\theta_{\text{turn}}) \quad (17)$$

where $\mathcal{R}(\theta_{\text{turn}})$ is the rotation matrix on scattering plane, with $\theta_{\text{turn}} \sim 2 \arctan \frac{\mu_{12}}{|\mathbf{v}_1 - \mathbf{v}_2|^2 b}$. The position vectors of m_1 and m_2 can be assumed to be unchanged (the scattering region is very small compared to r).

2.4 Scattering between two equal energy Keplerian orbits

The simplest scattering configuration between m_1 and m_2 in the potential of m_3 is one in which m_1 and m_2 move in Keplerian orbits and encounter at a location with distance r from m_3 . In this situation, the corresponding velocities and positions of m_1 and m_2 in the m_3 reference frame are

$$\mathbf{p}_1 = r(\cos v_1, \sin v_1, 0) \mathcal{E}(\omega, i, \Omega) \quad (18)$$

$$\mathbf{p}_2 = r(\cos v_2, \sin v_2, 0) \mathcal{E}(\omega, i, \Omega) \quad (19)$$

$$\mathbf{v}_1 = \pm \sqrt{\frac{\mu_{13}}{p_1}} (-\sin v_1, e_1 + \cos v_1, 0) \mathcal{E}(\omega, i, \Omega) \quad (20)$$

$$\mathbf{v}_2 = \pm \sqrt{\frac{\mu_{23}}{p_2}} (-\sin v_2, e_2 + \cos v_2, 0) \mathcal{E}(\omega, i, \Omega) \quad (21)$$

where $\mu_{j3} = G(m_j + M_3)$, p_j and e_j are the semi-latus rectum and eccentricity of m_j 's orbit, and $v_1 = v_2$ is the true anomaly that is obtained via $\cos v_j = (p_j/r - 1)/e_j$. $\mathcal{E}(\omega, i, \Omega)$ is the Euler rotation matrix with argument periastris ω , inclination i and longitude of the ascending node Ω .

Scatterings between an object (m_2) in a circular orbit and one in an eccentric orbit (m_1) with the same semi-major axis $a_1 = a_2 = r$ can be used to demonstrate most of the possible outcomes of the two-body coplanar scattering around a massive body. As shown in Figure 2, there are eight possible scatterings in this scenario due to different orbiting directions and relative positions of m_1 and m_2 . However, because of the symmetry of the orbits, there are scatterings that result in the same post-scattered orbits. Thus, only four unique scatterings exist. We label the symmetric scatterings with the same number labels as in Figure 2.

2.5 Valid parameter space

To safely ignore the gravity of m_3 during the scattering process between m_1 and m_2 , the timescale ratio $\tau_{\text{turn}}/\tau_{\text{orb}}$ needs to be much smaller than one,

$$\tau_{\text{turn}}/\tau_{\text{orb}} = \frac{1}{\pi} g \left(\sqrt{1 + \frac{b^2 v_\infty^4}{\mu_{12}^2}} \right) \left(\frac{\mu_3}{\mu_{12}} \right)^{1/2} \left(\frac{b v_\infty}{\sqrt{\mu_{12} r}} \right)^3 \ll 1. \quad (22)$$

Let us first consider the case of scattering between two objects in circular orbits; we then derive¹

$$b \ll \begin{cases} \left(\frac{9\pi^3}{8} \right)^{1/6} \left(\frac{m_{12}}{m_3} \right)^{1/6} R_{\text{Hill}} \sim 1.8 \left(\frac{m_{12}}{m_3} \right)^{1/6} R_{\text{Hill}}, & \text{retrograde} \\ \left(\frac{27\pi}{16} \right)^{1/6} R_{\text{Hill}} \sim 1.3 R_{\text{Hill}}, & \text{prograde} \end{cases} \quad (23)$$

The prograde case is the well-known Hill's radius that has been obtained in the same prograde configuration by balancing the gravity between the small objects m_1 , m_2 , and the massive object m_3 . For the retrograde case, where the relative velocity between m_1 and m_2 is larger than for the prograde case, one might expect that the scattering is faster due to the larger relative velocity. However, a_{hyp} is much larger than the one in the retrograde case. It takes a longer time for m_1 to fly out of the region $r < a_{\text{hyp}}(1 - e_{\text{hyp}}^2)$ to be an

¹ The Taylor expansion of $g(e_{\text{hyp}})$ at $e_{\text{hyp}}=1$ and $e_{\text{hyp}}=\infty$ are $g(e_{\text{hyp}}) \sim \frac{2}{3} - \frac{2(e_{\text{hyp}}-1)}{5} + \mathcal{O}((e_{\text{hyp}}-1)^2)$ and $g(e_{\text{hyp}}) \sim \frac{1}{e_{\text{hyp}}} + \frac{1-\log(2e_{\text{hyp}})}{e_{\text{hyp}}^3} + \mathcal{O}(\frac{1}{e_{\text{hyp}}^5})$, respectively. For prograde scatterings, v_∞ is b/r times of orbital velocity at r and $e_{\text{hyp}} \rightarrow 1$. For retrograde scatterings, v_∞ is two times of orbital velocity at r and e_{hyp} is very large that $g(e_{\text{hyp}})$ can be effectively expanded at infinity.

asymptotic straight line. Therefore, a smaller impact parameter is required for a two-body scattering approximation. Because these two cases give the extreme values of v_∞ (retrograde case gives the maximum value while prograde case gives the minimum value), for other scatterings with non-zero eccentricities, the critical impact parameter b is bracketed in between these two extreme values.

One should note that our numerical scattering experiments indicate that in the extreme case of prograde circular scattering with zero eccentricity, m_1 and m_2 may undergo continuous resonance scatterings so that no complete single scattering can be found in the continuous scattering patterns. The effective two-body scattering model in this paper can only be used for single scatterings in which m_1 and m_2 become unbound after the first encounter.

2.6 Post-scattering orbital calculations

The post-scattered velocities of m_1 and m_2 can be obtained by using Equation 16 to 17. Then the orbital parameters of m_1 and m_2 can be calculated by

$$a_i = \frac{\mu_{i3}}{\frac{2\mu_{i3}}{r_i} - v_i^2} \sim \frac{\mu_3}{\frac{2\mu_3}{r_i} - v_i^2} \quad (24)$$

$$e_i^2 = 1 + \frac{2l_i^2 \epsilon_i}{\mu_3^2} \quad (25)$$

where $l_i = \mathbf{r}_i \times \mathbf{v}_i$ and $\epsilon_i \sim -\frac{\mu_3}{2a_i}$ are the specific angular momentum and specific energy, respectively.

2.7 Verification of the analytical results with few-body scattering experiments

To validate the correctness of Equations 16-17, we set up a suite of scattering experiments with the few-body code SpaceHub (Wang et al. 2021b), and compare the numerical results with the analytical solutions. We perform our tests by adopting numerical values for the masses to represent the astrophysical scenario of stellar mass BHs scattering in the potential of a supermassive BH (Case A, AGN scenario), and of planets in the potential of a central star (Case B, planetary disk). The corresponding numerical values are, respectively, Case A: $m_1/m_3 = 10^{-8}$, $m_2/m_3 = 3 \times 10^{-7}$ and, and Case B: $m_1/m_3 = m_2/m_3 = 3 \times 10^{-6}$.

We verify the simplest retrograde circular scattering where both m_1 and m_2 orbit around m_3 in circular orbits in the opposite direction. We also test the results for scattering locations at different distances r from the central object m_3 to verify that length in this problem can be scaled freely with Hill radius.

For retrograde circular scatterings, the initial phase difference between m_1 and m_2 is π and the impact parameter (in this case, the semi-major axis difference) is d . For every single scattering, the simulation stops when the post-scattered relative phase between m_1 and m_2 becomes π again. We found that the semi-major axis difference may not be a good approximation of the impact parameter when $d < 10^{-4} R_{\text{Hill}}$ as indicated by Figure 3. Therefore, we run a set of simulations to obtain the relationship between the semi-major axis difference and the real impact parameter. The real impact parameters are calculated from the closest approach and relative velocity between m_1 and m_2 obtained from the simulations.

We do not test prograde scatterings with zero eccentricity because from the simulations we found that prograde circular scatterings result in continuous scatterings in which m_1 and m_2 continuously

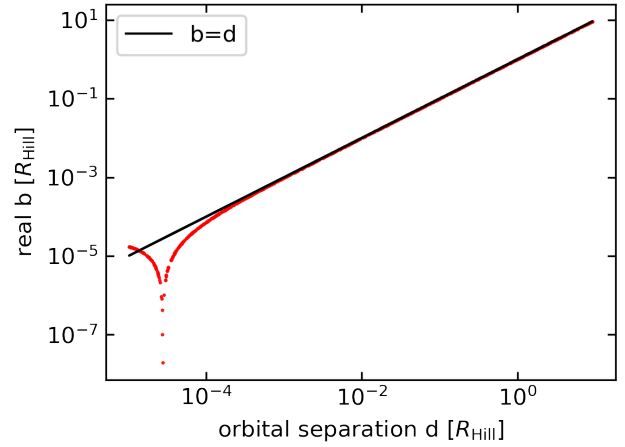


Figure 3. The relationship between semi-major axis difference and real impact parameter for circular orbit scatterings. The masses are $m_1 = 30M_\odot$, $m_2 = 1M_\odot$ and $m_3 = 10^8 M_\odot$. This relationship is scale-free with r .

swap their positions after the first close approach. This makes it difficult to distinguish individual scattering between these continuous scatterings. This limitation will be discussed in the last subsection.

Figure 4 shows, for the study case B, the comparison between the analytical approximation given by Equation 16, 17, 24, 25 and the numerical simulations. The left panels show the post-scattered eccentricity of m_1 and m_2 while the right panels indicate the post-scattered semi-major axis. This figure indicates that for retrograde circular scatterings with this mass combination, our analytical approximation can perfectly describe the two-body scattering for a region of impact parameters ranging from the minimum collision value (indicated by the vertical gray line) to the maximum value. The simulation results indicate that even for bigger impact parameters $b > b_{\text{valid,max}}$, the analytical approximation still describes the post-scattered eccentricity and semi-major axis very accurately.

Figure 5 shows the same comparison but for the larger mass set of case A. The post-scattered eccentricities and semi-major axis from the simulations fit the analytical results.

2.8 Impact parameter for a given closest approach

For a given closest approach R_{min} between m_1 and m_2 , the corresponding impact parameter for this closest approach is

$$b_{\text{min}} = R_{\text{min}} \sqrt{1 + \frac{2Gm_{12}}{v_\infty^2 R_{\text{min}}}}, \quad (26)$$

where v_∞ is the pre-scattering Keplerian velocity difference determined by the orbital parameters of m_1 and m_2 at the scattering location r with $a_1 = a_2 = r$ and $e_2 = 0$,

$$v_\infty^2 = \begin{cases} 2 \frac{Gm_3}{r} \left(1 - \sqrt{1 - e_1^2}\right) & \text{I\&II} \\ 2 \frac{Gm_3}{r} \left(1 + \sqrt{1 + e_1^2}\right) & \text{III\&IV.} \end{cases} \quad (27)$$

Then b_{min} can be expressed as

$$b_{\text{min}} = R_{\text{min}} \sqrt{1 + \frac{m_{12}}{m_3} \frac{r}{R_{\text{min}}} \frac{1}{\Delta_\pm}} \quad (28)$$

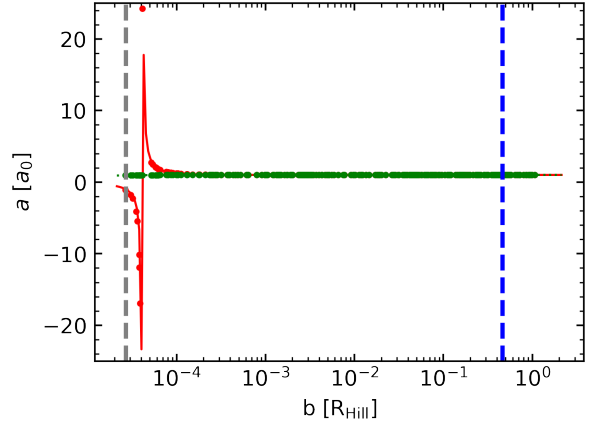
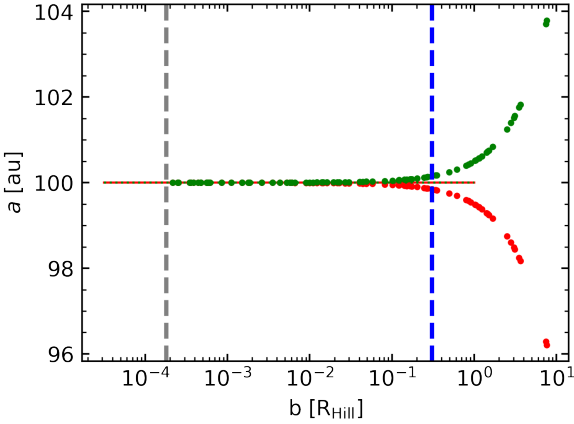
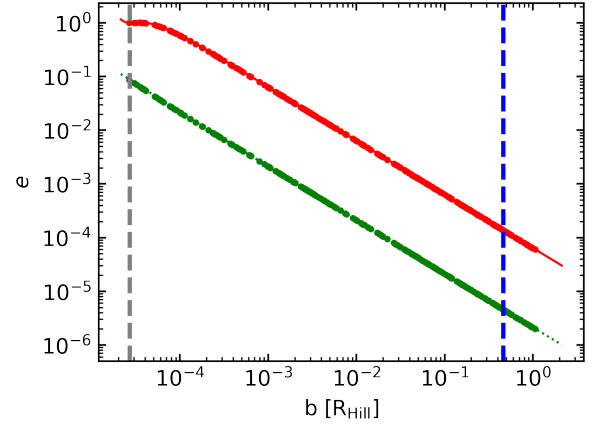
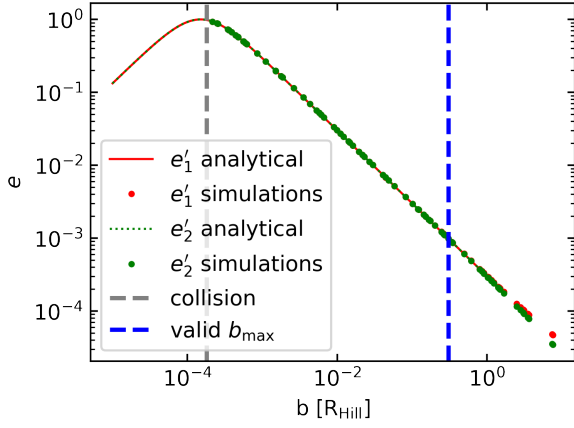


Figure 4. Post-scattered semi-major axis and eccentricity of circular retro-grade scatterings from simulations and analytical solution given by this paper. The scattering setup is $m_1 = 1M_\oplus$, $m_2 = 1M_\oplus$ and $m_3 = 1M_\odot$. The gray vertical lines indicate the impact parameter where m_1 and m_2 collide with each other (assuming earth-density planets). Vertical blue lines indicate the maximum impact parameter for which the analytical approximation is valid.

Figure 5. Same as Figure 4 but for case A where $m_1 = 1M_\odot$, $m_2 = 30M_\odot$ and $m_3 = 10^8M_\odot$.

where $\Delta_\pm = 1 \pm \sqrt{1 \pm e_1^2}$. This expression has the following limits:

$$b_{\min} = \begin{cases} \left(\frac{m_{12}}{m_3 \Delta_\pm} \right)^{1/2} \left(\frac{r}{R_{\min}} \right)^{1/2} R_{\min}, & r \gg r_c \\ R_{\min}, & r \ll r_c \end{cases} \quad (29)$$

where $r_c = R_{\min} \Delta_\pm \frac{m_3}{m_{12}}$. This is useful to obtain the corresponding impact parameter if a given closest approach is required (i.e. collision between m_1 and m_2 , or m_1 is tidally disrupted by m_2).

2.9 Ejection of the small object

The scattering between m_1 and m_2 can eject either m_1 and m_2 from the potential of m_3 . To calculate the critical impact b for ejecting m_1 , we can plug the Keplerian velocities into Equation 16-17 and Equation 24 and solve $e' = 1$. Solving the general case with arbitrary e_1 is not easy. However, it's relatively easy to get the solution in the limit of $e_1 \rightarrow 0$,

$$b/r = \begin{cases} \text{no solution, I\&II} \\ \pm \frac{\sqrt{7m_2^2 - 10m_1m_2 - m_1^2}}{4m_3}, & \text{III\&IV.} \end{cases} \quad (30)$$

This requires $-m_1^2 - 10m_1m_2 + 7m_2^2 > 0$ for a physical solution, that is $m_2/m_1 > \frac{5+4\sqrt{2}}{7}$. Similar results can be obtained in the limit of $e_1 \rightarrow 1$,

$$b/r = \begin{cases} \frac{2m_2 \pm \sqrt{(m_2 - m_1)(7m_2 + m_1)}}{2m_3}, & \text{I\&IV} \\ \frac{-2m_2 \pm \sqrt{(m_2 - m_1)(7m_2 + m_1)}}{2m_3}, & \text{II\&III} \end{cases} \quad (31)$$

The above conditions require the mass ratio m_2/m_1 to be

$$\begin{cases} 1 < \frac{m_2}{m_1}, & \text{I\&IV} \\ \frac{3 + 2\sqrt{3}}{3} < \frac{m_2}{m_1}, & \text{II\&III.} \end{cases} \quad (32)$$

2.10 Direct collision with the massive object

The scattering between m_1 and m_2 can also lead to a direct collision with m_3 . This case requires the post-encounter angular momentum of the small object to be zero.

Figure 6 illustrates the possible solution for the post-encounter angular momentum of small objects to be zero. If the initial position vector (unchanged during the scattering) lays outside of the allowed turning region, it is impossible for the post-encounter velocity vector to be aligned with the position vector. Thus, no solution can be obtained for $L' = 0$. If there are two intersections between the position

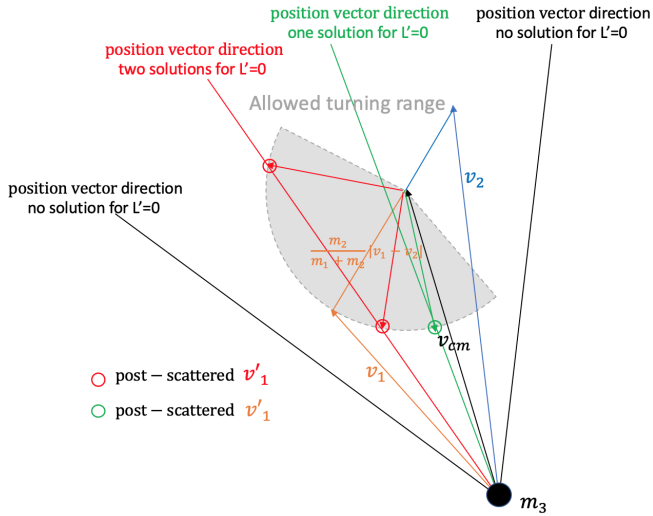


Figure 6. Illustration of scatterings that make the post-scattering angular momentum of m_1 , $L' = r' \times v'$, equal to zero. This would lead to m_1 colliding with m_3 . v_1 and v_2 are the initial velocities of m_1 and m_2 .

vector and the allowed turning region, there will be two solutions of b with $L' = 0$. Of course, if only one intersection can be found, then there is only one solution for b with zero post-encounter angular momentum.

The solutions for the four types of scattering are

$$b/r = \begin{cases} \text{no physical solution, I} \\ \frac{m_{12}}{2m_3}, \frac{m_2}{m_3} \frac{1}{\sqrt{1-e_1^2}}, \text{ II} : (\sqrt{1-e_1^2} \ll 1) \\ \frac{\sqrt{(3m_2-m_1)(m_1+m_2)}}{4m_3}, \text{ III} \\ \frac{m_2}{m_3} \frac{1}{\sqrt{1-e_1^2}}, \text{ IV} : (\sqrt{1-e_1^2} \ll 1) \\ \frac{\sqrt{(3m_2-m_1)(m_1+m_2)}}{4m_3}, \text{ IV} : (e_1 \ll 1) \end{cases} \quad (33)$$

Type I scatterings correspond to the case indicated by the black line (no solution). Type III and IV scatterings are indicated by the green line (one solution), while type II scatterings are represented by the red line (two solutions).

2.11 Examples of post-encounter orbital properties

In this section we show the post-encounter orbital properties for the two cases we introduced in Sec 2.7. These situations will be discussed further as astrophysical scenarios in Sec 3.

Figure 7 shows the post-scattered semi-major axis and eccentricity of the lighter object m_1 in case A for the different types of scatterings I, II, III, and IV shown in Figure 2. This case is a good example of scattering between a main sequence star and a stellar-mass black hole around a supermassive black hole. It indicates that type I and IV generally increase the semi-major axis of the lighter object m_1 until the impact parameter is down to $10^{-4}R_{\text{Hill}}$ where ejection of m_1 starts to appear. In case I, m_1 transfers energy to m_2 but gains angular momentum from m_2 . In case IV, m_1 transfers both energy and angular momentum to m_2 . For type II scatterings, the semi-major

axis of m_1 typically shrinks by a maximum factor of two if m_1 is in an extremely eccentric orbit. In this case, m_1 obtains energy from m_2 until ejection. For type III scatterings, low eccentricity orbits tend to increase the semi-major axis while high eccentricity orbits tend to decrease the semi-major axis.

For equal mass scatterings (case B), as shown in Figure 8, type I& II are symmetric between m_1 and m_2 in semi-major axis change, and type III&IV show similar behaviors. For type I and II scatterings, maximum semi-major axis and eccentricity are achieved at the same impact parameter b while in type III and type IV the maximum semi-major axis and maximum eccentricity occur at different impact parameters. Interestingly, for type I and II scatterings, low initial eccentricity cases can achieve maximum semi-major axis change with much larger impact parameters while in type III and IV scatterings, maximum semi-major axis change presents around $10^{-4}R_{\text{Hill}}$ for all initial eccentricities. Because the mass ratio between m_1 and m_2 is unity, based on the calculation in Section 2.9, no ejection can be obtained in the case.

3 APPLICATIONS

In the following, we will discuss the direct astrophysical implications of our analytical results for the two cases mentioned above: (i) Stellar-mass BH-star scatterings under the potential of a central SMBH (such as, for example, the disk of an AGN); (ii) planet-planet scattering in the potential of a host star, which is the typical situation of a planetary system with coplanar planetary orbits.

3.1 Micro-TDE in the presence of a central potential

If, during the scattering of a stellar-mass BH of mass m_2 and a main sequence star of mass m_1 and radius R_* , the star gets within a distance $r_t = R_*(\frac{m_1}{3m_3})^{1/3}$ of the BH, the tidal force from the BH will tidally disrupt the star, giving rise to long X-ray/gamma-ray flares (e.g. Perets et al. 2016).

Plug in r_t as R_{min} into Section 2.8, we can directly obtain the critical impact parameter for a micro-TDE

$$b_{\mu\text{TDE}} = R_{\mu\text{TDE}} \sqrt{1 + \frac{2G(m_{12})}{v_\infty^2 R_{\mu\text{TDE}}}}. \quad (34)$$

The cross-section of this micro-TDE can thus be estimated via

$$\begin{aligned} \sigma_{\mu\text{TDE}} &= \int_0^{b_{\mu\text{TDE}}} db = b_{\mu\text{TDE}} \\ &= \left(\frac{m_2}{3m_1}\right)^{1/3} R_* \sqrt{1 + \left(\frac{m_{12}}{m_3}\right) \left(\frac{3m_1}{m_2}\right)^{1/3} \frac{r}{R_*} \frac{1}{\Delta_\pm}}. \end{aligned} \quad (35)$$

This expression has the following limits:

$$\sigma_{\mu\text{TDE}} = \begin{cases} \left(\frac{m_{12}}{m_3\Delta_\pm}\right)^{1/2} \left(\frac{r}{R_{\mu\text{TDE}}}\right)^{1/2} R_{\mu\text{TDE}}, & r \gg r_c \\ R_{\mu\text{TDE}}, & r \ll r_c \end{cases} \quad (37)$$

where $r_c = R_* \Delta_\pm \left(\frac{m_3}{m_{12}}\right) \left(\frac{m_2}{3m_1}\right)^{1/3}$. Note that we have constructed a cross-section with units of length, rather than area, since our scattering problems are co-planar, and hence 2-dimensional.

Figure 9 shows the cross-section of the micro-TDE as a function of r for the four different types of scatterings shown in Figure 2, and for different orbital eccentricities of the star. Generally, the rate of micro-TDEs stays nearly constant if $r < r_c$ and increases as $r^{1/2}$

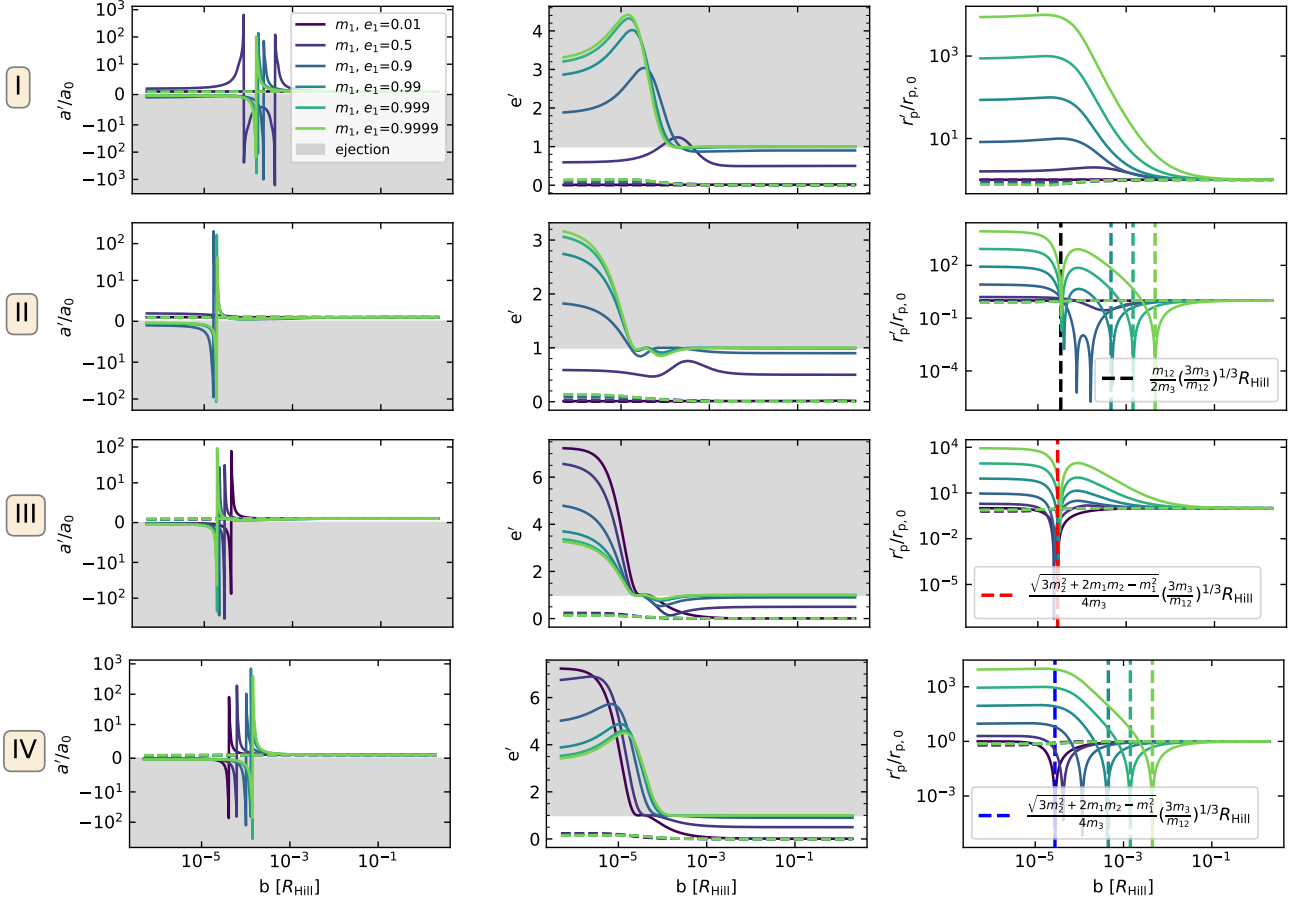


Figure 7. Post scattered orbital properties of m_1 (solid lines) and m_2 (dashed lines) from scatterings in the case with $m_1 = 1M_\odot$, $m_2 = 30M_\odot$ and $m_3 = 10^8M_\odot$.

Note that these curves are independent of the scattering position r to m_3 . Color dashed vertical lines that are not labeled are $\frac{m_2}{m_3} \frac{1}{\sqrt{1-e_1^2}} \left(\frac{m_3}{m_{12}}\right)^{1/3} R_{\text{Hill}}$.

in the region of $r > r_c$. In the outer region, the orbital velocity difference between m_1 and m_2 around the SMBH m_3 is significantly smaller than in the inner region, for both prograde scatterings (I and II) and retrograde scatterings (III and IV). Thus, the gravitational focusing effect in the larger r region is stronger. Since the star will be destroyed at the fixed radius $R_{\mu\text{TDE}}$, a stronger focusing effect in the larger r region leads to a larger cross-section of the micro-TDE. This focusing effect is extremely strong in prograde circular scatterings as shown in the upper two panels of Figure 9, which contributes most of the micro-TDEs in AGN disks.

3.2 Star ejection during a BH-star scattering

Instead of being disrupted by the stellar mass BH or the SMBH, the star could also be unbound from the SMBH by the BH during the scattering. To eject the star, the post-scattered semi-major axis as calculated from Equation 24 needs to be smaller than zero. Therefore, the cross-section of the star ejection is

$$\sigma_{\text{ej}} = \int_{\Sigma L_{\text{ej}}} db, \quad (38)$$

where L_{ej} encompasses all the regions in the parameter space of the impact parameter b that give a post-scattered eccentricity of the star smaller than zero (i.e. the post-scattered orbit is hyperbolic).

From Section 2.9, we then obtain that the cross-section of star ejection in the limit of $e_1 \rightarrow 0$ is

$$\sigma_{\text{ej}}(m_2/m_1 > \frac{5+4\sqrt{2}}{7}) = \quad (39)$$

$$\begin{cases} 0, \text{ I\&II} \\ \left(\frac{3m_3}{m_{12}}\right)^{1/3} \frac{\sqrt{7m_2^2 - 10m_1m_2 - m_1^2}}{4m_3} R_{\text{Hill}}, \text{ III\&IV} \end{cases} \quad (40)$$

$$\sigma_{\text{ej}}(1 < m_2/m_1 < \frac{5+4\sqrt{2}}{7}) = 0. \quad (41)$$

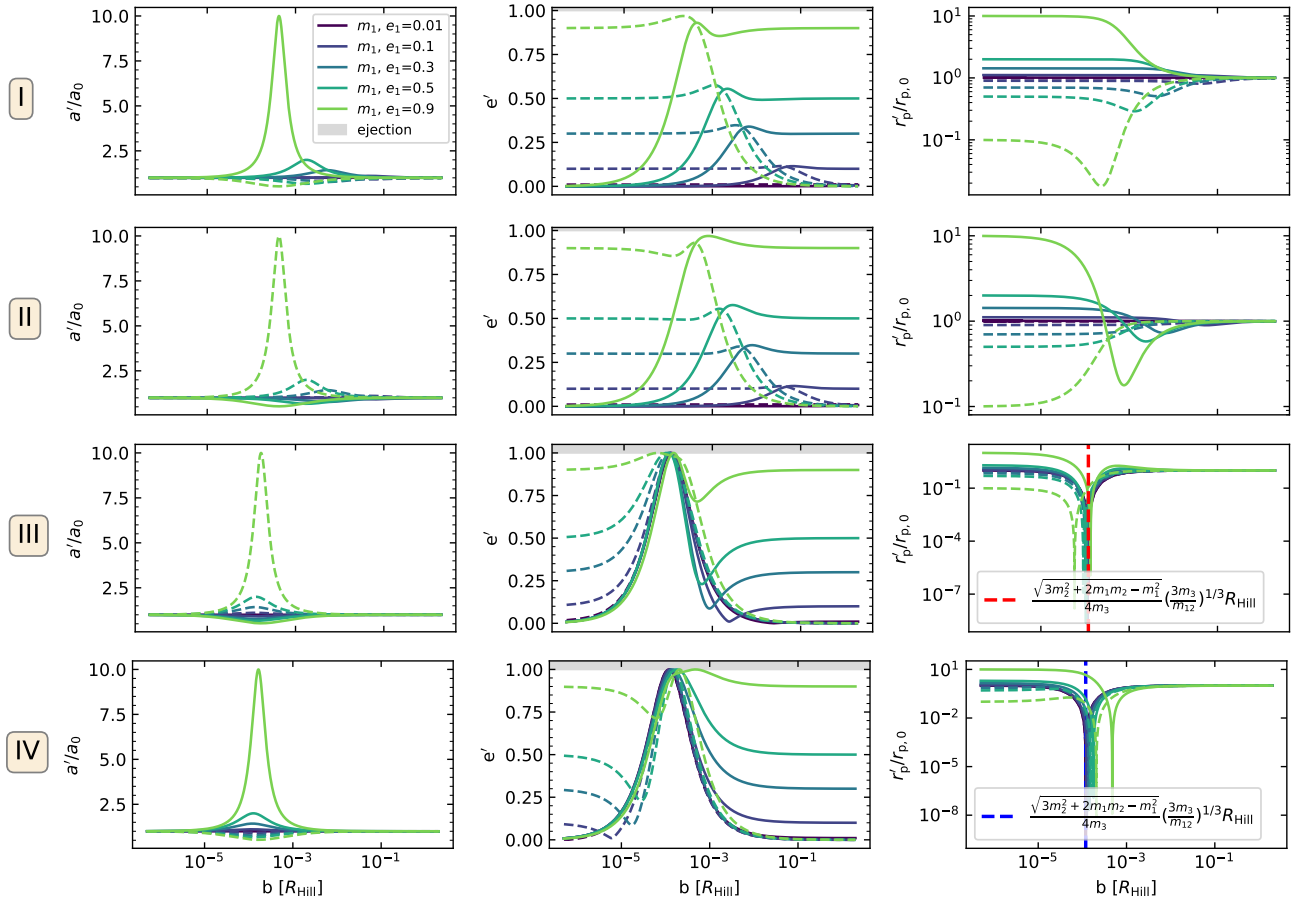


Figure 8. Similar to Figure 7. Post scattered orbital properties of m_1 and m_2 from scatterings in the case with $m_1 = 1M_{\oplus}$, $m_2 = 1M_{\oplus}$ and $m_3 = 1M_{\odot}$. The initial eccentricity of m_2 is always 0.

In the opposite limit of $e_1 \rightarrow 1$, the cross-section is

$$\sigma_{\text{ej}}\left(\frac{3+2\sqrt{3}}{3} < m_2/m_1\right) = \begin{cases} \frac{2m_2 + \sqrt{(m_2 - m_1)(7m_2 + m_1)}}{2m_3} \left(\frac{3m_3}{m_{12}}\right)^{1/3} R_{\text{Hill}}, \text{ I\&IV} \\ \frac{-2m_2 + \sqrt{(m_2 - m_1)(7m_2 + m_1)}}{2m_3} \left(\frac{3m_3}{m_{12}}\right)^{1/3} R_{\text{Hill}}, \text{ II\&III} \end{cases} \quad (42)$$

$$\sigma_{\text{ej}}\left(1 < m_2/m_1 < \frac{3+2\sqrt{3}}{3}\right) = \begin{cases} \frac{\sqrt{(m_2 - m_1)(7m_2 + m_1)}}{m_3} \left(\frac{3m_3}{m_{12}}\right)^{1/3} R_{\text{Hill}}, \text{ I\&IV} \\ 0, \text{ II\&III.} \end{cases} \quad (43)$$

Figure 10 shows the ejection cross-section of the star for different types of scatterings and different initial orbital eccentricities of the star. For prograde scatterings in type I and II, due to the low relative velocity between m_1 and m_2 in nearly circular orbits, the gravitational focusing between m_1 and m_2 can be very strong, and hence stars with low eccentricity orbits can be easily disrupted by the BH before they acquire enough energy to be ejected. Only stars in a highly eccentric orbit, requiring less energy for ejection, can hence be ejected before the disruption. This is consistent with what we obtained from Equation 42.

For retrograde scatterings in type III and IV, due to the large

relative velocity between m_1 and m_2 , gravitational focusing is much weaker than for prograde scatterings. Thus an encounter with a much smaller impact parameter can be achieved without star disruption. Therefore, even stars with low eccentricity orbits can be ejected by the stellar mass BH. The horizontal dashed lines show the approximation obtained from Equation 42, indicating that the ejection cross-section is effectively independent of r . The sharp vertical cutoffs mark where micro-TDEs take over. In the left small r region, the required impact parameter for star ejection is smaller than the micro-TDE impact parameter. Therefore, the star will be tidally disrupted by the stellar mass BH and hence there is no ejection.

3.3 Star tidally disrupted by the central SMBH (TDE)

‘Standard’ TDEs, in which the star is disrupted by the SMBH in quiescent galactic nuclei, have been extensively studied in the literature. The resulting flares are widely used to study the properties of the SMBH (mass, spin) as well as the populations of the host galactic nucleus (e.g. Bloom et al. 2011). TDEs in AGN disks are due to: either a) a ‘standard’ TDE in a nucleus where the TDE orbit crosses an AGN disk (Kathirgamaraju et al. 2017; Chan et al. 2019) or b) due to a dynamical interaction between 2 or 3 bodies in the AGN

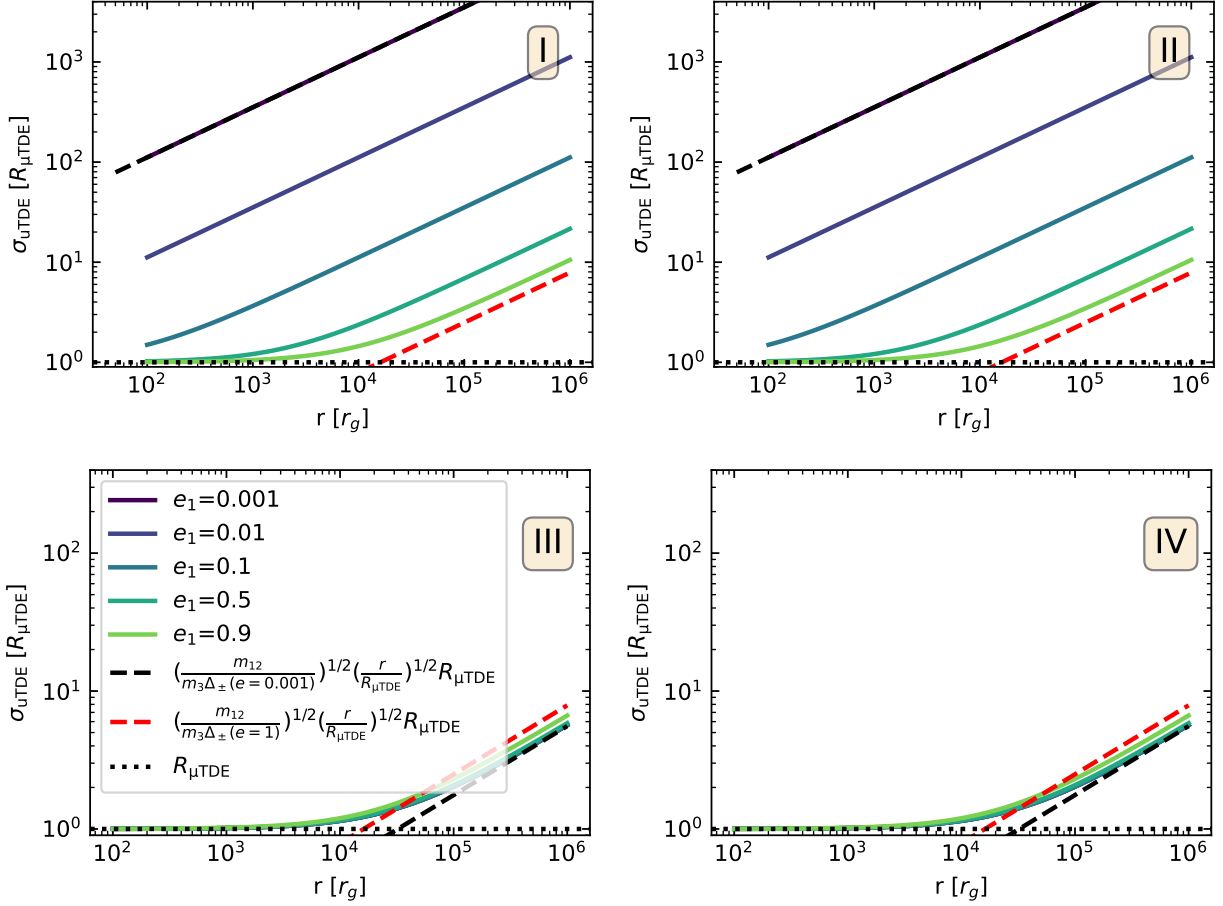


Figure 9. Micro-TDE (disrupted by the stellar mass BH) cross-section as a function of r for different types of scatterings. The mass of the central SMBH is $10^8 M_\odot$ and the mass of the star is M_\odot and the mass of the stellar mass BH that tidally disrupts the star is $30M_\odot$.

disk that scatters the star onto the SMBH (McKernan et al. 2022)². In case a) the TDE is due to the standard 2-body scattering into the loss cone independent of the disk and the rate of occurrence is the same as regular TDEs for that galaxy type. In case b) the TDE is due to 2-body or 3-body scattering in the AGN disk and the rate of occurrence of such events is a function of disk size and the number of embedded objects within it. TDEs in AGN disks can create unique signatures because of the presence of the disk and must correspond to a source of AGN variability (Graham et al. 2017). Note that in the discussion below we assume that scattered stars in AGN disks are $\sim 1M_\odot$. Since stars on prograde orbits within AGN disks can very rapidly grow to $O(100M_\odot)$ (Cantiello et al. 2021), this corresponds to assuming the scattered star lies on an embedded retrograde orbit.

In our scattering model, the scatterings between m_1 and m_2 can result in a star orbit with a very small pericenter. The SMBH could tidally disrupt the star if this enters the tidal disruption radius of the SMBH,

$$R_{\text{TDE}} \sim \left(\frac{m_3}{3m_1} \right)^{1/3} R_*. \quad (44)$$

² This picture is complicated by the very different evolution of stars embedded in AGN disks (Cantiello et al. 2021; Jermyn et al. 2021) and which could have a significant impact on dynamical encounters within the disk and the disk itself (Jermyn et al. 2022).

The cross-section for these TDEs can be obtained via

$$\sigma_{\text{TDE}} = \int_{\Sigma L_{\text{TDE}}} db, \quad (45)$$

where ΣL_{TDE} encompasses all the regions in the parameter space of the impact parameter b that give a post-scattered star orbit with pericenter smaller than R_{TDE} .

Solving for the post-scattered pericenter $r_{p,1} = a_1(1-e_1) = R_{\text{TDE}}$ analytically is not straightforward. However, as shown in Section 2.10, it is relatively easy to solve for $r_{p,1} = 0$. These solutions indicate the most probable impact parameter for TDE to happen. The TDE cross-section can be found by solving $r_{p,1} = a_1(1-e_1) = R_{\text{TDE}}$. But we have not been able to find an analytical solution for it. However, we can find a scaling for the TDE cross-section. That is $\sigma_{\text{TDE}} \propto \sqrt{r}$.

Figure 11 shows the SMBH TDE cross-section as a function of the distance r from the SMBH. These TDEs are completely forbidden in the inner region of the AGN disk in our setup since they require a high eccentricity of the stellar orbit. However, this is almost impossible to obtain from the scattering between a $1M_\odot$ star and a $30M_\odot$ BH, as evinced by Equation 16-17 and shown in Figure 7. SMBH TDEs start to emerge around $10^4 r_g$ where the post-scattered eccentricity of the star orbit could reach unity. Type II and type III scatterings contribute most of the TDEs.

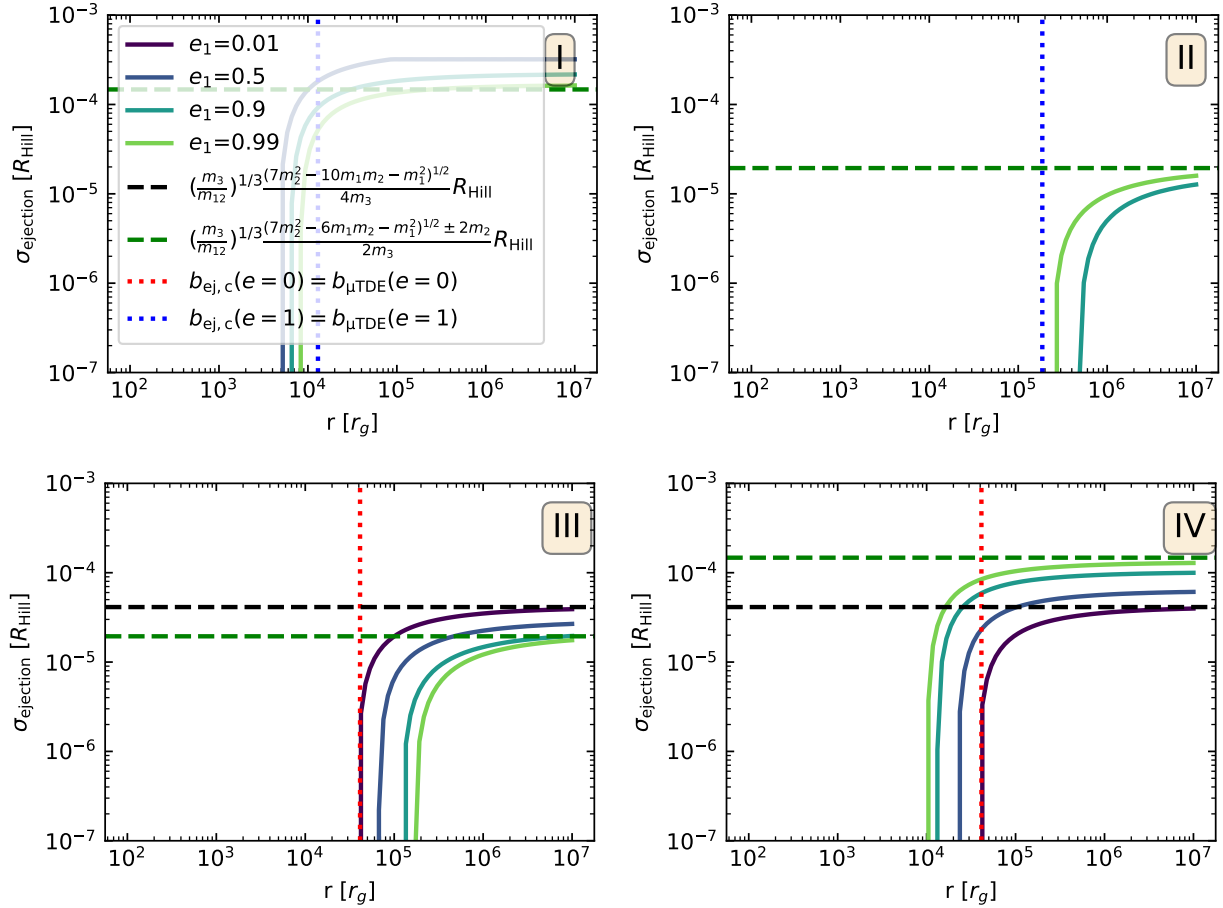


Figure 10. Similar to Figure 9, but for the star ejection. The horizontal dashed lines show the approximation from Equation 42. The vertical dotted lines indicate the critical r , where the star gets tidally disrupted by the stellar mass black hole before it gets ejected.

3.4 Free-floating and high eccentricity planets

For planetary systems with multiple planets, the interactions between planets may lead to chaotic evolution of the planet orbits, causing planet orbits to cross. Once the planet orbits can cross each other, the scattering between planets can significantly change the architecture of the planetary system. This scattering process will last until the two planet orbits become well separated or one of the planets is ejected from the system by a very close encounter (Chatterjee et al. 2008; Li et al. 2014; Pu & Lai 2021; Li et al. 2021). In the latter scenario, the leftover planet is usually associated with high eccentricity (Lin & Ida 1997; Ford & Rasio 2008; Jurić & Tremaine 2008; Spurzem et al. 2009; Wang et al. 2020; Li et al. 2020) and the ejected planet becomes a free-floating planet (Sumi et al. 2011; Beaugé & Nesvorný 2012) unless it is re-captured by other planetary systems. This is one of the potential mechanisms that can be used to explain the high eccentricity of exoplanets and free-floating planets.

Similar to the star-BH ejection case, the cross-section of the planet ejection is well described by Equation 39 to 43. Figure 12 shows the cross-section of the planet ejection between an Earth-mass planet and a Jupiter-mass planet. For prograde scatterings, it is difficult to get planet ejection from circular planet orbits, only high eccentricity orbits have the chance to be ejected from the system. The corresponding impact parameters between the two planets are roughly $10^{-3} R_{\text{Hill}} - 10^{-1} R_{\text{Hill}}$. For retrograde scatterings, even circular planet orbits have the chance to be ejected, although retrograde scatterings

are much rare in planetary systems. Figure 12 also indicates that the ejections happen in the outer region of the planetary system. If the scatterings are too close to the host star, planet-planet collisions will occur.

Although Figure 8 shows equal mass, and equal orbital energy scatterings (ejection never happens), we can see from the trend if we compare it with Figure 7 that the leftover planet will become very eccentric once the other planet gets ejected from the system. This agrees with the general picture of planet-planet scattering in the literature.

4 CONCLUSIONS

4.1 Summary

We have presented a fully analytical solution to the 2-body scattering problem in the presence of a central gravitational potential, in planar geometry. Our solution is highly accurate under the condition that the duration of the scattering event (as measured by the turning time of the scatterer's orbits) is much smaller than the orbital time in the potential of the third body. The valid parameter space in the circular scattering limit is given by Equation 23, where for prograde scatterings, the impact parameter between two small objects needs to be smaller than the (well-known) Hill's radius, and for retrograde scatterings, the impact parameter needs to be an even smaller number

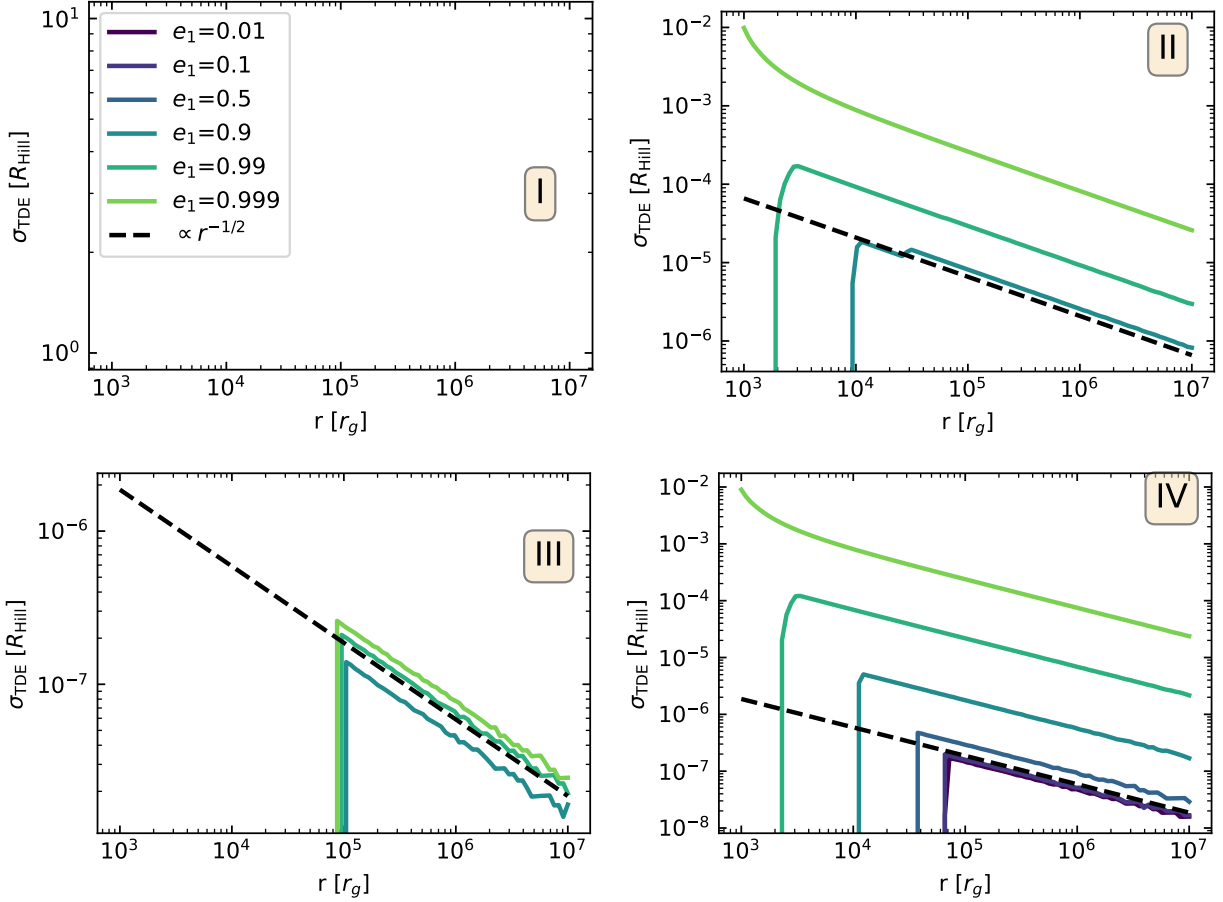


Figure 11. TDE (disrupted by the SMBH) cross-section as a function of r for different types of scatterings as shown in Figure 2

$\sim (m_{12}/m_3)^{1/6} R_{\text{Hill}}$. For other scatterings with non-zero eccentricities, the critical impact parameter b is between these two extreme values.

We tested the validity of our analytical solution via scattering experiments, and, as illustrative examples, we applied the analytical solution to compute cross sections of astrophysical events in planar geometry under the presence of a third massive body providing the central potential. These include scattering events between stars and black holes in the SMBH potential of AGN disks, which lead to micro-TDEs, where the star is disrupted by the stellar BH it is scattering with, and SMBH TDEs, where the scattered star ends up on a very eccentric orbit that leads it to a plunge within the tidal disruption radius of the SMBH, yielding an AGN-TDE. An accurate cross-section of these events is provided in Section 3. More generally, our analytical formulation can be very effective at saving computational time, while obtaining accurate results, in planar 2-body scatterings under the presence of a massive third body. From the calculated critical impact parameters and cross-sections, we can summarize some interesting results (Due to the geometry of the 2-D scattering setups, all cross-sections listed below are in length units).

- Micro TDEs in AGN disks are most contributed from prograde scatterings between a star and a stellar-mass black hole in low eccentricity orbits (hundreds to thousands of geometry cross-section of the tidal radius). For retrograde scatterings, if the scattering position is $< 10^4 r_g$, the cross-section of the micro-TDE is basically the geometry cross-section of the tidal radius.

- The cross-section of star ejection (by a stellar-mass black hole) in AGN disks is roughly $10^{-5} - 10^{-4} R_{\text{Hill}}$, effectively independent of the scattering position with respect to the SMBH, although, in the inner region of the disk, the star gets tidally disrupted instead.

- Tidal disruption events by SMBH are relatively rare compared to micro-TDE in AGN disks. The cross-section is roughly $10^{-7} - 10^{-4} R_{\text{Hill}}$ for orbits without extreme initial eccentricity. The cross-section scales with scattering position in $r^{1/2}$. The inner region of the disk is nearly forbidden for macro-TDEs due to the micro-TDEs.

- For planet-planet ejection, equal mass scatterings are more difficult to produce ejected planets than unequal mass scatterings. The cross-section for planet ejection is roughly $10^{-2} - 10^{-1} R_{\text{Hill}}$. The inner region is also forbidden for planet ejection due to the planet-planet collision.

4.2 Caveats

We emphasize that the analytical approximation we derived in the paper is meant to describe the two-body *single* scattering around a massive object. However, for prograde circular scatterings, where the two small objects orbit around the massive object in the same direction, multiple continuous scatterings can occur. In the scattering parameter space i.e. the space of impact parameter and relative velocity, these multiple scatterings can be hard to distinguish, e.g. the orbital turning from one scattering is not finished when the following scattering begins. The equations we derived require every

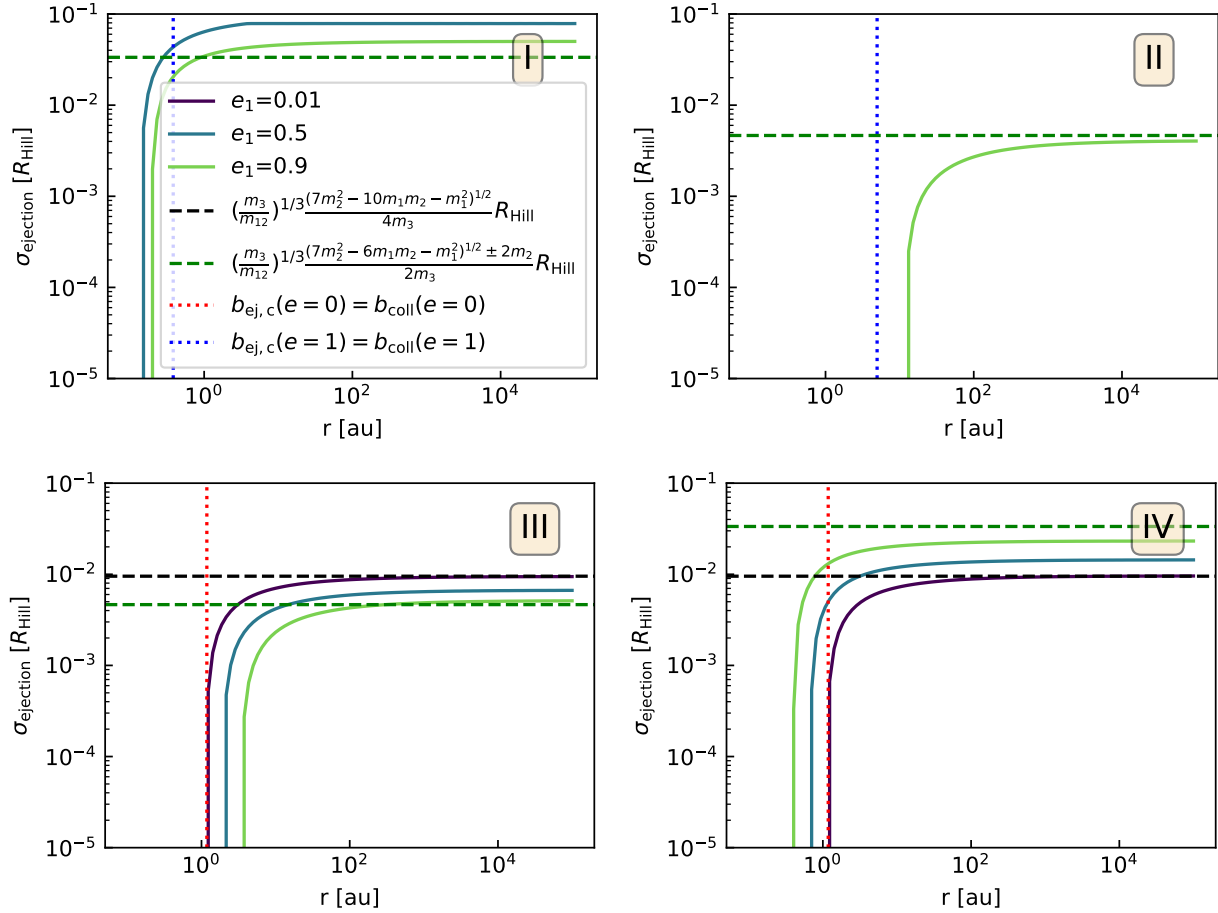


Figure 12. Similar to Figure 10, but the setup is an Earth-mass planet encounter with a Jupiter-mass planet under the potential of a solar mass star.

single scattering to be finished, i.e. the turning process needs to be complete. Thus, Equation 16 to 17 cannot properly describe close multiple scatterings for which each individual scattering cannot be discriminated. However, via numerical experiments, one can identify the regions of the parameter space where resonant scattering (multiple scatterings) does not occur, so that the equations derived here can be properly used.

For the environments of AGN disks, two-body scatterings can be complicated due to the existence of the gaseous environment. These gas effects may lead to very different post-scattered results, thus significantly changing the cross-section/rate of the events we discussed in this paper. The descriptions and cross-section/rate estimates of the various astrophysical events made in this paper are all based on an assumption of no gas effects. More sophisticated computations, inclusive of gas effects, need to be performed to give more accurate cross-sections/rates of the various events.

All calculations after Sec 2.8 are based on the assumption of equal energy orbit scatterings. This is the most probable situation for scatterings between two Keplerian orbits. For more general cases, another free parameter indicating the energy ratio between the two planet orbits is required in all the expressions of the calculated critical impact parameters and cross-sections.

ACKNOWLEDGEMENTS

BM and KESF are supported by NSF AST 1831415 and Simons Foundation grant 533845. RP acknowledges support by NSF award AST-2006839. ZZ acknowledges support by NASA award 80NSSC22K1413. YW thanks Scott Tremaine for reminding us of the work of Opik in the 1950s, and Dong Lai for helpful discussion. YW and BZ are supported by Nevada Center for Astrophysics.

DATA AVAILABILITY

The data underlying this article will be shared on reasonable request to the corresponding author.

References

- Bartos I., Kocsis B., Haiman Z., Márka S., 2017, *ApJ*, **835**, 165
- Beaugé C., Nesvorný D., 2012, *ApJ*, **751**, 119
- Bloom J. S., et al., 2011, *Science*, **333**, 203
- Cantiello M., Jermyn A. S., Lin D. N. C., 2021, *ApJ*, **910**, 94
- Carusi A., Valsecchi G. B., Greenberg R., 1990, *Celestial Mechanics and Dynamical Astronomy*, **49**, 111
- Chan C.-H., Piran T., Krolik J. H., Saban D., 2019, *ApJ*, **881**, 113
- Chatterjee S., Ford E. B., Matsumura S., Rasio F. A., 2008, *ApJ*, **686**, 580
- Ernst Ö., 1976, *Interplanetary Encounters: Close-Range Gravitational Interactions*. Elsevier Scientific Pub, Amsterdam

- Evans C. R., Kochanek C. S., 1989, *ApJ*, **346**, L13
- Fabj G., Nasim S. S., Caban F., Ford K. E. S., McKernan B., Bellovary J. M., 2020, *MNRAS*, **499**, 2608
- Ford E. B., Rasio F. A., 2008, *ApJ*, **686**, 621
- Graham M. J., Djorgovski S. G., Drake A. J., Stern D., Mahabal A. A., Glikman E., Larson S., Christensen E., 2017, *MNRAS*, **470**, 4112
- Greenberg R., Carusi A., Valsecchi G. B., 1988, *Icarus*, **75**, 1
- Jermyn A. S., Dittmann A. J., Cantiello M., Perna R., 2021, *ApJ*, **914**, 105
- Jermyn A. S., Dittmann A. J., McKernan B., Ford K. E. S., Cantiello M., 2022, *ApJ*, **929**, 133
- Jurić M., Tremaine S., 2008, *ApJ*, **686**, 603
- Kathirgamaraju A., Barniol Duran R., Giannios D., 2017, *MNRAS*, **469**, 314
- Kennedy G. F., Meiron Y., Shukirgaliyev B., Panamarev T., Berczik P., Just A., Spurzem R., 2016, *MNRAS*, **460**, 240
- Kremer K., Lombardi James C. J., Lu W., Piro A. L., Rasio F. A., 2022, arXiv e-prints, p. [arXiv:2201.12368](https://arxiv.org/abs/2201.12368)
- Li G., Naoz S., Valsecchi F., Johnson J. A., Rasio F. A., 2014, *ApJ*, **794**, 131
- Li D., Mustill A. J., Davies M. B., 2020, *MNRAS*, **496**, 1149
- Li J., Lai D., Anderson K. R., Pu B., 2021, *MNRAS*, **501**, 1621
- Lin D. N. C., Ida S., 1997, *ApJ*, **477**, 781
- McKernan B., Ford K. E. S., Lyra W., Perets H. B., 2012, *MNRAS*, **425**, 460
- McKernan B., Ford K. E. S., Cantiello M., Graham M., Jermyn A. S., Leigh N. W. C., Ryu T., Stern D., 2022, *MNRAS*, **514**, 4102
- Perets H. B., Li Z., Lombardi James C. J., Milcarek Stephen R. J., 2016, *ApJ*, **823**, 113
- Phinney E. S., 1989, in Morris M., ed., Vol. 136, The Center of the Galaxy. p. 543
- Pu B., Lai D., 2021, *MNRAS*, **508**, 597
- Rees M. J., 1988, *Nature*, **333**, 523
- Ryu T., Perna R., Wang Y.-H., 2022, *MNRAS*, **516**, 2204
- Samsing J., et al., 2020, arXiv e-prints, p. [arXiv:2010.09765](https://arxiv.org/abs/2010.09765)
- Spurzem R., Giersz M., Heggie D. C., Lin D. N. C., 2009, *ApJ*, **697**, 458
- Stone N. C., Metzger B. D., Haiman Z., 2017, *MNRAS*, **464**, 946
- Sumi T., et al., 2011, *Nature*, **473**, 349
- Valsecchi G. B., Froeschlé C., Gonczi R., 1997, *Planet. Space Sci.*, **45**, 1561
- Wang Y.-H., Perna R., Leigh N. W. C., 2020, *MNRAS*, **496**, 1453
- Wang Y.-H., Perna R., Armitage P. J., 2021a, *MNRAS*, **503**, 6005
- Wang Y.-H., Leigh N. W. C., Liu B., Perna R., 2021b, *MNRAS*, **505**, 1053
- Wang Y.-H., McKernan B., Ford S., Perna R., Leigh N. W. C., Low M.-M. M., 2021c, *ApJ*, **923**, L23
- Yang Y., Bartos I., Haiman Z., Kocsis B., Márka S., Tagawa H., 2020, arXiv:2003.08564,

This paper has been typeset from a $\text{\TeX}/\text{\LaTeX}$ file prepared by the author.